ARTICLE

Check for updates

Suppression of the transition to superconductivity in crystal/glass high-entropy alloy nanocomposites

Xiaofu Zhang[1,2,6✉], Rui Shu [3,6], Huanlong Liu[4], Anna Elsukova[3], Per O. Å. Persson[3], Andreas Schilling [4✉], Fabian O. von Rohr [5✉] & Per Eklund [3✉]

Superconducting high entropy alloys (HEAs) may combine extraordinary mechanical properties with robust superconductivity. They are suitable model systems for the investigation of the interplay of disorder and superconductivity. Here, we report on the superconductivity in $(TaNb)_{1-x}(ZrHfTi)_x$ thin films. Beyond the near-equimolar region, the films comprise hundreds-of-nanometer-sized crystalline grains and show robust bulk superconductivity. However, the superconducting transitions in these nanocomposites are dramatically suppressed in the near-equimolar configurations, i.e., $0.45 < x < 0.64$, where elemental distributions are equivalently homogeneous. Crystal/glass high entropy alloy nanocomposite phase separation was observed for the films in the near-equimolar region, which yields a broadened two-step normal to superconducting transition. Furthermore, the diamagnetic shielding in these films is only observed far below the onset temperature of superconductivity. As these unusual superconducting transitions are observed only in the samples with the high mixing entropy, this compositional range influences the collective electronic properties in these materials.

[1] State Key Laboratory of Functional Materials for Informatics, Shanghai Institute of Microsystem and Information Technology, Chinese Academy of Sciences (CAS), Shanghai 200050, China. [2] CAS Center for Excellence in Superconducting Electronics, Shanghai 200050, China. [3] Thin Film Physics Division, Department of Physics, Chemistry, and Biology (IFM), Linköping University, Linköping 58183, Sweden. [4] Department of Physics, University of Zürich, Winterthurerstrasse 190, CH-8057 Zürich, Switzerland. [5] Department of Chemistry, University of Zürich, Winterthurerstrasse 190, CH-8057 Zürich, Switzerland. [6] These authors contributed equally: Xiaofu Zhang, Rui Shu. ✉email: zhangxf@mail.sim.ac.cn; schilling@physik.uzh.ch; fabian.vonrohr@uzh.ch; per.eklund@liu.se

Controlling the structure and crystallinity of functional materials is key to enhancing their performance in applications. High-entropy alloys (HEAs)[1–3] are composed of five or more multiprincipal elements in near-equimolar proportions, and exhibit remarkable mechanical and functional properties. The term "high-entropy alloy"[4], though debated, stems from the original proposal that the presence of multiprincipal elements can increase the configurational entropy of mixing. If this entropy increase is sufficient to overcome the enthalpies of compound formation, regular crystallographic lattices can then be stabilized, such as body-centered cubic (*bcc*), face-centered cubic (*fcc*), and hexagonal closed-packed (*hcp*). Once these distorted lattices collapse, such solid solutions then transform either into amorphous alloys or into crystal/glass composites. Amorphous alloys, or metallic glasses, are metallic alloys with a metastable amorphous structure[5,6]. Their formation typically requires a negative heat of mixing, an atomic mismatch greater than 12%, and three or more elements. Engineering of amorphous grain boundaries can enhance the stability against grain growth. Nanocrystalline/amorphous nanocomposite thin films synthesized by physical vapor deposition have been widely studied for their mechanical[7,8] and electrical properties[9,10], but a multiprincipal-element material comprising glass-forming elements can induce a quasiductile deformation with near-theoretical strength, as exemplified by the addition of Fe-Si-B to polycrystalline CrFeCoNi[11].

This types of HEA/amorphous-alloy nanocomposites offer possibilities for tailoring electronic properties, including superconductivity. Generally, in non-magnetic superconductors, a weak disorder will not lead to a substantial change of the transition temperature to superconductivity[12]. In 2014, a superconducting HEA of TaNb-Zr-Hf-Ti, i.e., consisting primarily of 4d and 5d elements, was discovered[13]. A variety of studies have been performed on HEA superconductors since then [14–23], in part because the combined electronic and mechanical properties found in HEAs suggest their use as functional materials in applications[21]. In nanocrystalline/amorphous nanocomposites, however, nanoscale grains with thin amorphous grain boundaries will form a granular electronic system. It is then necessary to take the Coulomb repulsion effect into consideration, together with the strong disorder, which in turn may lead to suppression of superconductivity. The formation of metallic glasses and HEA/amorphous-alloy nanocomposites could therefore impose dramatic effects on superconductivity, stressing the need to elucidate the electronic properties and superconducting behavior in this emerging class of nanocomposite materials. To this end, we have synthesized $(TaNb)_{1-x}(ZrHfTi)_x$ thin films with the nominal composition x varying from 0.22 to 0.75 by using magnetron sputtering (see Supplementary Table 1).

Results

Microstructure. Figure 1a shows the X-ray diffractograms of the $(TaNb)_{1-x}(ZrHfTi)_x$ films as function of x, where all samples show a *bcc* structure. When x increases from 0 to 1, the 110 Bragg peaks, located around 37°, is gradually shifted to lower 2θ angles (larger d spacings). The calculated lattice parameters increase from $a = 3.36$ Å to 3.49 Å (Supplementary Fig.1). SEM images of the surface morphology are shown in Supplementary Fig. 2. In the composition region $0.42 \leq x \leq 0.66$, the films present a weak 110 peak superimposed with a broad amorphous halo, indicating that these films are composed of an amorphous phase and a nanocrystalline *bcc* phase. To further investigate the structure of the films, plan-view transmission electron microscopy was performed for $(TaNb)_{0.4}(ZrHfTi)_{0.6}$ and $(TaNb)_{0.6}(ZrHfTi)_{0.4}$. Figure 1b shows a plan-view Scanning transmission electron

microscopy (STEM) image of the $(TaNb)_{0.4}(ZrHfTi)_{0.6}$ ($x = 0.6$) film. The selected-area electron diffraction (SAED) pattern (Fig. 1d) acquired from the corresponding circled area in Fig. 1b, consists of an amorphous bright ring together with some bright spots from the polycrystalline regions. Two more SAED patterns shown in Fig. 1e and f acquired individually from the circled crystalline and glass regions (Fig. 1b), indicate a crystal/glass nanocomposite structure for the $x = 0.6$ film, where elongated grains with a lateral width of ~250 nm are embedded in the matrix full of nanoscale granular domains (Fig. 1f). A high-magnification STEM image (Fig. 1g) shows the lattice structure for two *bcc*-phase crystals and a grain boundary from the crystalline region in Fig. 1f. The composition in the crystalline and amorphous regions is homogeneous since no apparent compositional fluctuations can be observed by energy-dispersive X-ray spectroscopy (EDX) elemental mapping (Supplementary Fig. 3).

For $x = 0.4$, in contrast, a fully crystalline microstructure with grain size larger than 1 µm is observed (Fig. 1h). The needle-like sub-grains, are semi-coherently arranged, parallel to each other, as shown in the higher magnification STEM image (Fig. 1i) and in the lattice resolved STEM image (Fig. 1j). The SAED pattern (Fig. 1h, inset) shows diffraction spots that can be assigned to a *bcc* phase, which is supported by the Fast Fourier Transform (FFT) diffraction pattern in Fig. 1j.

This series of films were synthesized under the kinetically limited vapor-growth condition where a large cooling rate of ~10^6 Ks^{-1}, a few orders of magnitude than conventional HEAs bulk materials, limits the kinetics of long-range diffusion and favors condensed atoms formed fine-grained (often metastable) crystals or into an amorphous structure. Moreover, for the $(TaNb)_{1-x}(ZrHfTi)_x$ films with x from 0.42 to 0.6, the high-configurational entropy ($\triangle S_{mix}^{conf}$) in near-qual atomic composition yields lattice distortion and sluggish diffusion effects. Both can seriously hinder the nucleation and grain coarsening driven by surface atom diffusion. The higher enthalpy of mixing (ΔH_{mix}) in range of $0.42 \leq x \leq 0.64$, also increases the activation energy of crystallization (Supplementary Fig. 4a), compared to x outside this range. Both of above effects result in the formation of glassy proportion and the crystal-glass nanocomposite for the $(TaNb)_{1-x}(ZrHfTi)_x$ films where $0.42 \leq x \leq 0.64$. Furthermore, the crystallinity of those films could be improved by post-annealing (Supplementary Fig. 5).

Complementary electronic transport and magnetization studies. Superconductivity is a macroscopic quantum state, which is phenomenologically characterized by zero resistivity and the Meissner effect. To show the onset of superconductivity and the effects by the suppression of the formation of crystal/glass phases in HEAs, we performed complementary electronic transport and magnetization measurements to characterize the normal-to-superconducting transitions for all these films. Figure 2 present the onsets of superconductivity for six selected samples ($x = 0.22$, 0.30, 0.40, 0.50, 0.60, and 0.69), the resistive normal-to-superconducting transitions, together with magnetization measurements in a static external field of 2 mT with zero-field cooling (ZFC) and field cooling (FC) protocols (reciprocating sample option). Far away from the high-configurational-entropy region ($0.42 \leq x \leq 0.64$), we observe rather sharp transitions, where the transition region in temperature is less than 0.1 K wide (Fig. 2a–c, f). The onsets of superconductivity of these films are also clearly revealed by the ZFC curves. The normal-to-superconducting transitions for the near-equimolar films, by contrast, first take place at T_c^{on} (where the $\rho(T)$ dependence starts to deviate from the metallic behavior), and then reveal a kink instead of sharp superconducting transition. The true zero-resistivity
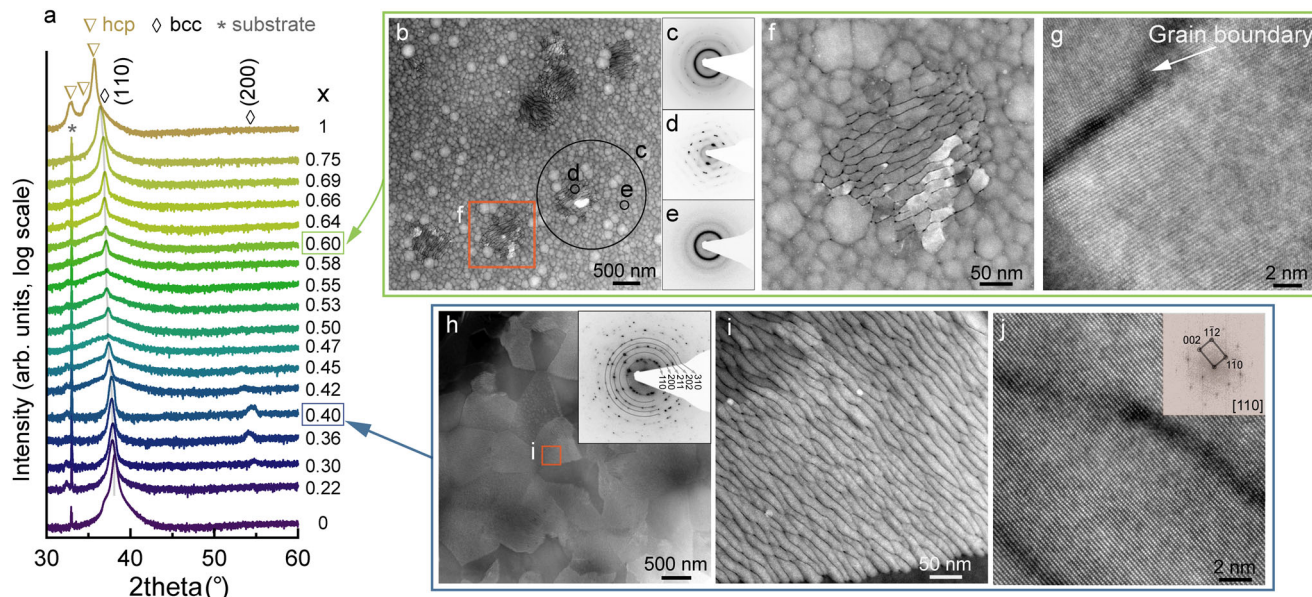
Fig. 1 Microstructure of the (TaNb)$_{1-x}$(ZrHfTi)$_x$ films. a $\theta-2\theta$ X-ray diffractograms of the (TaNb)$_{1-x}$(ZrHfTi)$_x$ films deposited on Si (100) substrate as a function of x, from 0 to 1. **b** HAADF-STEM images of (TaNb)$_{0.4}$(ZrHfTi)$_{0.6}$, revealing a crystal/glass nanocomposite structure. **c** SAED pattern from the corresponding circled area in **b**. **d**, **e** SAED patterns from the corresponding circled regions in **b**, respectively. **f** Magnified view from **b**. **g** HAADF-STEM image of crystalline region. **h–j**, HAADF-STEM images of (TaNb)$_{0.6}$(ZrHfTi)$_{0.4}$, showing a crystalline microstructure. The inset on top of **h** shows the SAED pattern from selected area in **h**. **i** Higher magnification of the boxed area in **h**. **f** Lattice resolved HAADF-STEM image. The inset is the corresponding fast Fourier transform (FFT) image, showing a *bcc* phase structure with <110> zone axis.

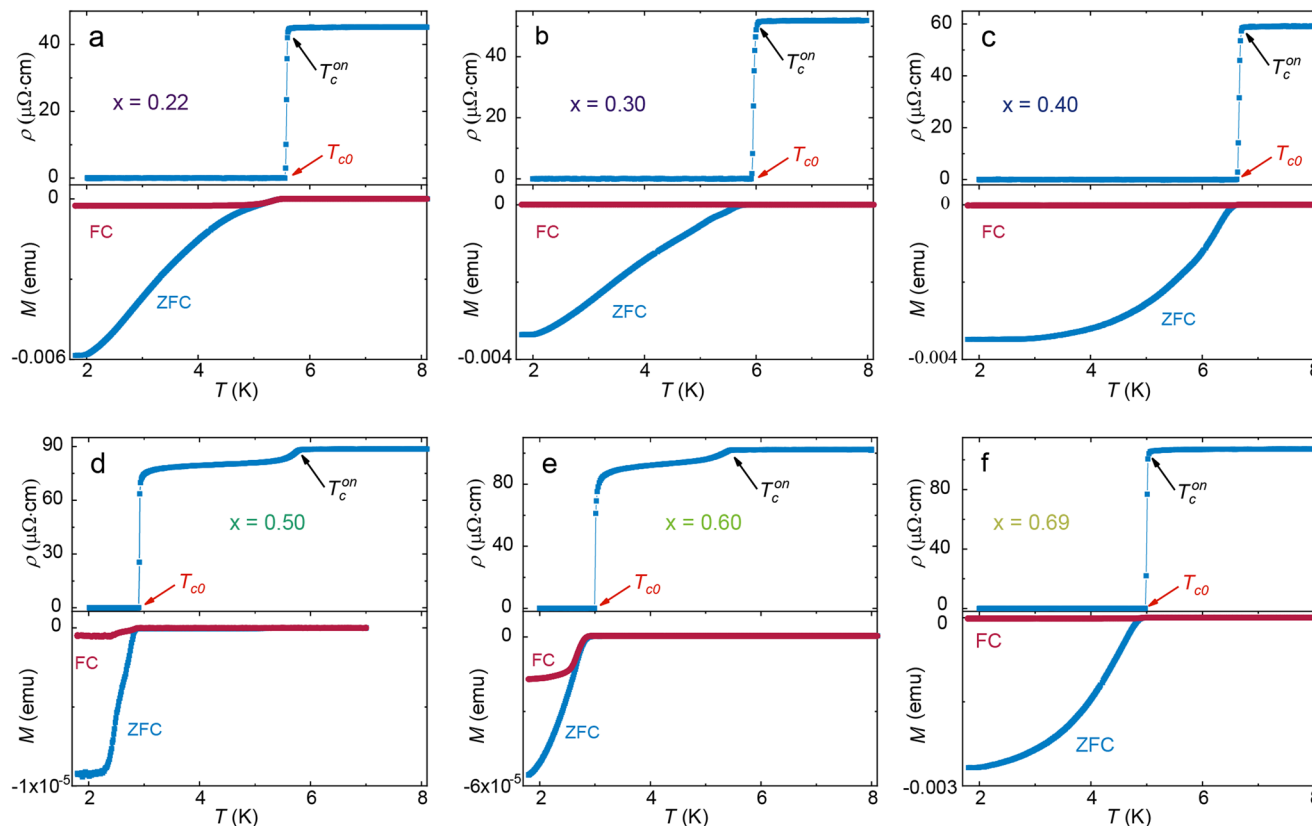**Fig. 2 Normal to superconducting phase transitions of the (TaNb)$_{1-x}$(ZrHfTi)$_x$ films. a–f** The temperature dependence of the resistivity and the magnetization curves for both zero-field cooling and field cooling (2 mT) for $x = 0.22$, 0.30, 0.40, 0.50, 0.60, and 0.69, respectively.
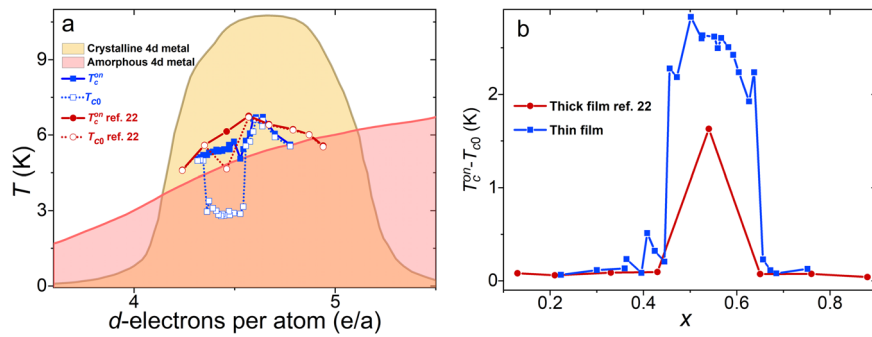
Fig. 3 Suppression of superconductivity in the near-equimolar region. a The valence-electron concentration dependence of the onset temperature and the zero-resistivity temperature of superconductivity. The valence-electron concentration as a function of composition is shown in the Supplementary information (Supplementary Fig. 4c). The black dashed line schematically shows the T_c dependence of $(TaNb)_{1-x}(ZrHfTi)_x$ crystalline films on the valence-electron concentration. **b** The transition width between T_c^{on} and T_{c0} as a function of ZrHfTi composition.

superconducting state, however, can only be established at a lower temperature T_{c0} ~3 K, forming a surprisingly broad transition region to superconductivity and a two-step normal to superconducting transition. Consistent with the $\rho(T)$ dependence, the transition to maximum diamagnetism revealed by the ZFC data is also suppressed to T_{c0}. Moreover, the total magnetic moment of these near-equimolar films under ZFC is found to be two orders of magnitude smaller than that in the other films, indicating the reduced superconducting volume fraction and the existence of non-superconducting phases. Even for $x = 0.42$ and 0.66, although the transport measurements show a sharp transition to zero-resistivity superconducting state at T_c^{on}, the drop on the ZFC curves demonstrate that a large fraction of the non-superconducting phases eventually enters into superconducting state with further decreasing temperature only below ~3 K (Supplementary Fig. 6).

To uncover the suppression of superconductivity in these near-equimolar films, we here summarize all the resulting T_c^{on} and T_{c0} in Fig. 3 as a function of the electron/atom (e/a) ratio (black squares and red circles, respectively). Additional data from thicker films from ref. [22] are also included. As a comparison, the trend lines of the critical temperatures for the transition metals and their alloys in crystalline form (magenta region) and in amorphous forms (blue region) are also shown[24,25]. The onset of superconductivity temperature T_c^{on} in the HEA films is between the two benchmark lines, showing a similar dependence on valence-electron concentration as the maximal T_c line of crystalline alloys, as according to the Matthias rule[24]. The valence-electron concentration dependence of T_c^{on} is consistent with the results from the crystalline HEAs[14], demonstrating that the decreasing resistivity at T_c^{on} originates from the embedding crystalline nano-grains in the near-equimolar region. However, due to the poor fraction of nano-grains in these near-equimolar films (Fig. 1b), a zero-resistive superconducting path is not yet established, which in turn leads to only a slight reduction of resistivity. Generally, we would expect that these T_{c0} should locate near the amorphous alloys benchmark as a result of the dominating constituting amorphous aggregations. The T_{c0} dependence on valence-electron concentration, however, shows a sudden drop near the near-equimolar region, with electron/atom ratios ranging from 4.36 to 4.54, where T_{c0} for all near-equimolar films are suppressed down to a surprisingly constant temperature around 3 K, irrespective of the valence-electron concentration, as it is shown in Fig. 3. It is also noteworthy that, although these films in the near-equimolar region are constituted by nanocrystal/glass phases, the T_{c0} for the zero-resistivity is suppressed even below the trend line for amorphous superconductors[25], evoking a consideration of enhanced suppression beyond the amorphous transitional-metal alloys.

To gain more insight into the two-step superconducting transitions, we have performed systematic magnetotransport measurements for all films with external magnetic fields up to 9 T perpendicular to the film surface. Figure 4 is a plot of the dependence of the resistivity on applied magnetic fields in the vicinity of the superconducting transitions for the corresponding films analogous to Fig. 2. For increasing magnetic field, the superconducting transitions are gradually shifted to lower temperatures and the transition region is slightly broadened. By defining the critical temperature as the temperature where the resistivity falls to half of the normal-state resistivity, the field dependence of the critical temperature for selected films beyond the near-equimolar region is shown in the Supplementary Information (Supplementary Fig. 7a). For films with $x = 0.4$, the suppression of superconductivity by the magnetic field, and the shifts of the superconducting transitions, are more pronounced than for films for $x > 0.66$. By fitting the $B_{c2}(T)$ dependence with the Werthamer–Helfand–Hohenberg theory in the dirty limit[26,27], we note that all the corresponding zero-temperature upper critical fields $B_{c2}^{WHH}(0)$ for $x > 0.66$ are larger than the Pauli paramagnetic limiting field B_c^P [28,29]. For $x = 0.69$ and 0.75, the critical fields $B_{c2}^{WHH}(0)$ are 10.9 and 8.5 T, while the $B_c^P = 1.86T_c$ are 9.3 and 7 T, respectively. In the near-equimolar region, the field-dependent transitions show systematic shifts to lower temperatures, while the shapes of the transitions remain the same. The field dependence of T_c^{on} and T_{c0} are summarized in the Supplementary Information (Supplementary Fig. 7b).

Discussion

A key question with respect to the broad suppressed resistive region near T_c is its origin. An at first sight trivial possibility is the presence of two distinct and entirely unrelated components with different critical temperatures in the equimolar region. A further question we will consider is whether the broad suppressed resistive region it is due to the lack of global coherence (Bosonic scenario), or if it is induced by the suppressed formation of Cooper pairs (Fermionic scenario)[30–33], which both are also valid scenarios that would lead to the emergence of such a kink region in the resistance at the normal-to-superconducting transition. As we shall below, the latter scenario naturally leads to a picture with two components on the one hand, which are, on the other hand, closely linked to one another.

When temperature decreases from the metallic normal state, Cooper pairs start to form firstly at T_c^{on} in these nano-crystalline granules. As it is revealed by the residual resistance between T_c^{on} and T_{c0}, the more crystalline fraction (more crystalline granules), the less residual resistance below T_c^{on}. With the temperature
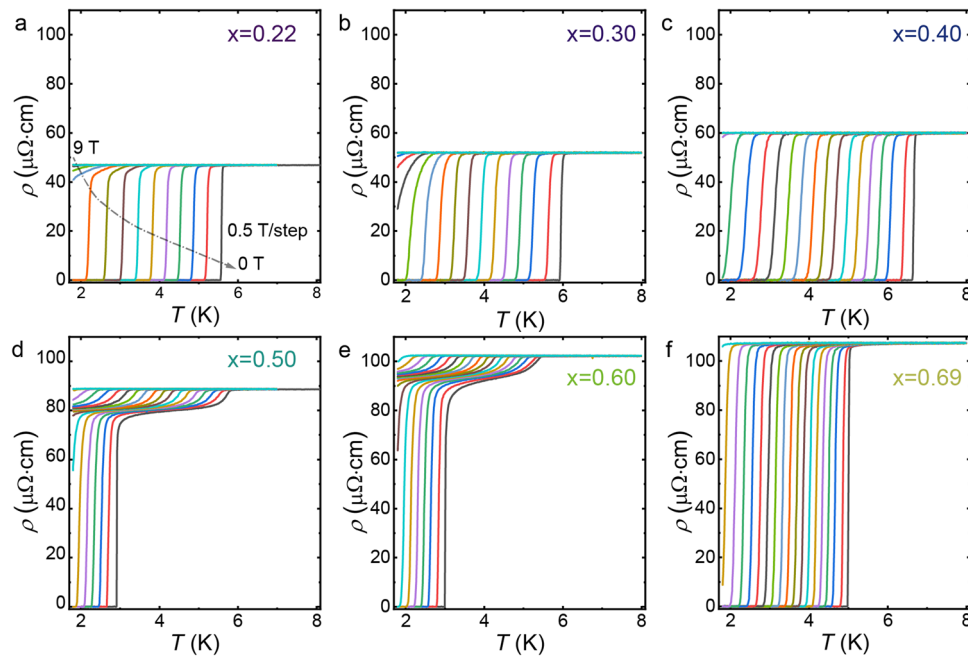
Fig. 4 Magnetotransport properties of (TaNb)$_{1-x}$(ZrHfTi)$_x$ films. a–f The temperature dependence of the resistivity in magnetic fields from 0 to 9 T for $x = 0.22$, 0.30, 0.40, 0.50, 0.60, and 0.69, respectively.

further decreasing, the total resistance decreases as these pairs diffuse from the superconducting domains into the nearby superconducting or normal domains[30], and the phase coherence among superconducting domains strengthens continuously. However, due to the reduced portions of the nano-crystalline granules, it is then not sufficient to establish the global superconducting coherence for films in the near-equimolar region, forming a percolative scenario below T_c^{on}. Only when the temperature is lower than T_{c0} (the onset of superconductivity in amorphous aggregations), where all amorphous aggregations also transition into superconducting state, the global phase coherence is then established, and the system shows zero resistivity, leading to a Bosonic suppression mechanism[31–33]. This Bosonic scenario successfully explains the two-step superconducting transitions that have also been observed for Mo$_2$C crystals[34], boron-doped granular diamond[35], Nb$_{1-x}$Cu$_x$ binary alloys ($x > 0.54$)[36], and Nb-islands based superconducting-normal-superconducting nanostructures[37]. However, the Bosonic scenario alone is not able to sufficiently describe the transition in the near-equimolar HEAs. Despite the T_c^{on} values of these films in the near-equimolar region are composition dependent, the values of T_{c0} are a nearly identical value. Intuitively, one would deduce that a new phase with a specific composition is formed, which has a T_c around 3 K. However, this possibility can be excluded since no extra phase was detected in the film with composition in the near-equimolarq region (X-ray diffraction (XRD) analysis, Fig. 1). Moreover, the uniform morphology characteristic of these films in equimolar region is that the size of amorphous aggregations size can be down to a few nanometers, which is close to the critical size d_c for granular superconductors, for instance, $d_c \sim 6$ nm for Nb[38].

Due to the formation of nanocrystal/glass dual phases in these near-equimolar HEAs films, an additional size effect must be considered for these nanoscale amorphous aggregations. Since the size of the constituting amorphous aggregations is close to the corresponding zero-temperature Ginzburg-Landau coherence length[22], superconductivity in these films hinges on the formation of stabilized Cooper pairs. As a result of the decrease in the diffusive motion of electrons impeded by the reduced dimensionality of amorphous aggregations together with strong

structural disorder, which strengthens the effective Coulomb repulsion, it would then overpower the attractive interaction necessitated for Cooper pairs[39]. For an individual aggregation, due to the reduced dimensionality induced energy levels spacing $\delta\varepsilon$ of electrons inside the nanoscale aggregations, it will be non-superconducting once $\delta\varepsilon$ is larger than the superconducting energy gap $\triangle$, $\delta\varepsilon = \left(N_0 d^3\right)^{-1} > \triangle$, where N_0 is the density of states at the Fermi level and d^3 is the volume of the nano-aggregations[39]. Despite the fact that the onset temperature of electron-pair condensation as a function of the valence-electron concentration is reached, the condensation of Cooper pairs in the nanoscale aggregations is still limited by the critical size as a result of the reduced dimensions. This, in turn, leads to a Fermionic scenario in which limited-size-induced pairing fluctuations suppress the formation of Cooper pairs[40–42]. Here, upon decreasing the temperature in the near-equimolar HEAs films below T_c^{on}, the $\triangle$ starts to be non-zero for the homogeneously distributed HEA crystals. However, the electrons cannot condense into Cooper pairs due to the reduced size in these amorphous aggregations. By further decreasing the temperature, the $\triangle$ will increase significantly as $T \ll T_c^{on}$, and as soon as $\delta\varepsilon < \triangle$ is fulfilled, all the amorphous aggregations will enter the superconducting state, with a rapid drop of resistivity and emerging diamagnetism. This would also explain why the T_{c0} are nearly identical in the near-equimolar region.

Finally, to further elaborate on the influence of amorphous aggregations on superconductivity, the field-dependent normal to superconducting transitions of as-deposited and post-annealed films with $x = 0.47$ and 0.50, which are mostly constituted by the amorphous aggregations, are presented in Supplementary Fig. 8. Due to the facilitated crystallinity, the superconductivity between T_{c0} and T_c^{on} for $x = 0.47$ films is then enhanced. However, since there still exists a substantial amorphous aggregation (Supplementary Fig. 5), the second transition at $T_{c0} \sim 3$K persists. Especially for the $x = 0.5$ film, where the amorphous halo is nearly completely suppressed (Supplementary Fig. 5), a direct normal to superconducting transition is eventually observed for its post-annealed film (Supplementary Fig. 8). it confirms that the

superconducting transition at T_{c0} indeed originates from the amorphous aggregation phase.

Conclusions

In conclusion, we have studied the formation of nonequilibrium crystal/glass nanocomposites in magnetron-sputtering-deposited near-equimolar $(TaNb)_{1-x}(ZrHfTi)_x$ films. In the regular poly-crystalline HEAs, with bcc structure and outside the near-equimolar region, the $(TaNb)_{1-x}(ZrHfTi)_x$ films show robust superconductivity, similar to the superconductivity in amorphous-alloy systems, in which the onset of superconductivity is dependent on the valence-electron concentration. In the crystal/glass nano-composites in the near-equimolar region, however, the Coulomb repulsion effects may be enhanced due to the formation of nanoscale amorphous aggregations together with a strong struc-tural disorder, and the effective attraction interaction between electron pairs is likely significantly suppressed in such a way that the nano-amorphous aggregations act as non-superconducting granules. The zero-resistivity temperatures, along with the asso-ciated diamagnetism, are then suppressed far below the T_c^{on}.

Methods

Materials synthesis. The $(TaNb)_{1-x}(ZrHfTi)_x$ films were deposited by direct current (DC) co-sputtering (PVD Products, Inc.) with two three-inch compound TaNb and ZrHfTi targets (99.9%, MaTeck GmbH) at room temperature with non-intentional heating. The films were deposited in an Ar atmosphere at a pressure of 3 mTorr, controlling the DC power of each target separately. The stoichiometries were then measured by the Energy-Dispersive X-ray spectroscopy. Silicon (100) substrates terminated by Si_3N_4 with a size of 10×10 mm² were cleaned sequen-tially with acetone and ethanol in an ultrasonic bath for 15 min, and finally blow-dried with nitrogen gas. The substrates were electrically floating. The resulting thickness of these films is ~300 nm.

Structural characterization. XRD was carried out on a PANalytical X'Pert powder diffractometer with a Cu source ($\lambda_{K\alpha} \approx 1.5406$ Å) operating at 45 kV/40 mA. STEM combined with high-angle annular dark field imaging (STEM-HAADF) and EDX analysis with a Super-X EDX detector was performed in the Linköping mono-chromated, high-brightness, double-corrected FEI Titan³, operated at 300 kV. The specimens for TEM examination were made by mechanical grinding, followed by Ar^+-ion milling, which was performed on a Gatan 691 Precision Ion Polishing Systems cooling with liquid nitrogen. Initially, the incident angle and energy of Ar^+ ions were set at 9° and 4.2 KeV, respectively. During the final step, they were reduced to 6° and 3.0 KeV, respectively.

Resistivity measurement. Resistivity measurements were performed in a Quan-tum Design PPMS (9 T) using a standard four-probe technique. The sheet resis-tance was measured by the van der Pauw method. Contacts were made by using a 25-μm-diameter aluminum wire. The wires were contacted to the films by using the TPT wire bonder.

Data availability

The data that support these findings are available from the corresponding authors on request.

References

1. Yeh, J.-W. et al. Nanostructured high-entropy alloys with multiple principal elements: novel alloy design concepts and outcomes. *Adv. Eng. Mater.* **6**, 299–303 (2004).
2. Cantor, B., Chang, I. T. H., Knight, P. & Vincent, A. J. B. Microstructural development in equiatomic multicomponent alloys. *Mater. Sci. Eng. A* **375–377**, 213–218 (2004).
3. George, E. P., Raabe, D. & Ritchie, R. O. High-entropy alloys. *Nat. Rev. Mater.* **4**, 515–534 (2019).
4. Miracle, D. B. & Senkov, O. N. A critical review of high entropy alloys and related concepts. *Acta Mater.* **122**, 448–511 (2017).
5. Klement, W., Willens, R. H. & Duwez, P. Non-crystalline Structure in Solidified Gold–Silicon Alloys. *Nature* **187**, 869–870 (1960).
6. Inoue, A. Stabilization of metallic supercooled liquid and bulk amorphous alloys. *Acta Mater.* **48**, 279–306 (2000).
7. Vepřek, S. The search for novel, superhard materials. *J. Vac. Sci. Technol. Vac. Surf. Films* **17**, 2401–2420 (1999).
8. Mayrhofer, P. H., Mitterer, C., Hultman, L. & Clemens, H. Microstructural design of hard coatings. *Prog. Mater. Sci.* **51**, 1032–1114 (2006).
9. Eklund, P. et al. Structural, electrical, and mechanical properties of nc-TiC/a-SiC nanocomposite thin films. *J. Vac. Sci. Technol. B Microelectron. Nanometer Struct. Process. Meas. Phenom.* **23**, 2486–2495 (2005).
10. Lewin, E., Wilhelmsson, O. & Jansson, U. Nanocomposite nc-TiC/a-C thin films for electrical contact applications. *J. Appl. Phys.* **100**, 054303 (2006).
11. Wu, G. et al. Crystal–glass high-entropy nanocomposites with near theoretical compressive strength and large deformability. *Adv. Mater.* **32**, 2002619 (2020).
12. Anderson, P. W. Theory of dirty superconductors. *J. Phys. Chem. Solids* **11**, 26–30 (1959).
13. Koželj, P. et al. Discovery of a superconducting high-entropy alloy. *Phys. Rev. Lett.* **113**, 107001 (2014).
14. Rohr, F., von, Winiarski, M. J., Tao, J., Klimczuk, T. & Cava, R. J. Effect of electron count and chemical complexity in the Ta-Nb-Hf-Zr-Ti high-entropy alloy superconductor. *Proc. Natl Acad. Sci.* **113**, E7144–E7150 (2016).
15. Jasiewicz, K., Wiendlocha, B., Korbeń, P., Kaprzyk, S. & Tobola, J. Superconductivity of $Ta_{34}Nb_{33}Hf_8Zr_{14}Ti_{11}$ high entropy alloy from first principles calculations. *Phys. Status Solidi RRL – Rapid Res. Lett.* **10**, 415–419 (2016).
16. Guo, J. et al. Robust zero resistance in a superconducting high-entropy alloy at pressures up to 190 GPa. *Proc. Natl Acad. Sci.* **114**, 13144–13147 (2017).
17. Vrtnik, S. et al. Superconductivity in thermally annealed Ta-Nb-Hf-Zr-Ti high-entropy alloys. *J. Alloy. Compd.* **695**, 3530–3540 (2017).
18. Yuan, Y. et al. Superconducting $Ti_{15}Zr_{15}Nb_{35}Ta_{35}$ high-entropy alloy with intermediate electron-phonon coupling. *Front. Mater.* **5**, (2018).
19. von Rohr, F. O. & Cava, R. J. Isoelectronic substitutions and aluminium alloying in the Ta-Nb-Hf-Zr-Ti high-entropy alloy superconductor. *Phys. Rev. Mater.* **2**, 034801 (2018).
20. Stolze, K., Tao, J., von Rohr, F. O., Kong, T. & Cava, R. J. Sc–Zr–Nb–Rh–Pd and Sc–Zr–Nb–Ta–Rh–Pd high-entropy alloy superconductors on a CsCl-type lattice. *Chem. Mater.* **30**, 906–914 (2018).
21. Jin, K. & Bei, H. Single-phase concentrated solid-solution alloys: bridging intrinsic transport properties and irradiation resistance. *Front. Mater.* **5**, id.26 (2018).
22. Zhang, X. et al. Preparation and characterization of high-entropy alloy $(TaNb)_{1-x}(ZrHfTi)_x$ superconducting films. *Phys. Rev. Res.* **2**, 013375 (2020).
23. Sun, L. & Cava, R. J. High-entropy alloy superconductors: status, opportunities, and challenges. *Phys. Rev. Mater.* **3**, 090301 (2019).
24. Matthias, B. T. Empirical relation between superconductivity and the number of valence electrons per atom. *Phys. Rev.* **97**, 74–76 (1955).
25. Collver, M. M. & Hammond, R. H. Superconductivity in 'amorphous' transition-metal alloy films. *Phys. Rev. Lett.* **30**, 92–95 (1973).
26. Werthamer, N. R., Helfand, E. & Hohenberg, P. C. Temperature and purity dependence of the superconducting critical field, H_{c2}. III. Electron spin and spin-orbit effects. *Phys. Rev.* **147**, 295–302 (1966).
27. Baumgartner, T. et al. Effects of neutron irradiation on pinning force scaling in state-of-the-art Nb_3Sn wires. *Supercond. Sci. Technol.* **27**, 015005 (2013).
28. Clogston, A. M. Upper limit for the critical field in hard superconductors. *Phys. Rev. Lett.* **9**, 266–267 (1962).
29. Chandrasekhar, B. S. A note on the maximum critical field of high-field superconductors. *Appl. Phys. Lett.* **1**, 7–8 (1962).
30. Sacépé, B. et al. Localization of preformed Cooper pairs in disordered superconductors. *Nat. Phys.* **7**, 239–244 (2011).
31. Sacépé, B., Feigel'man, M. & Klapwijk, T. M. Quantum breakdown of superconductivity in low-dimensional materials. *Nat. Phys.* **16**, 734–746 (2020).
32. Beloborodov, I. S. Suppression of superconductivity in granular metals. *Phys. Rev. Lett.* **92**, 207002 (2004).
33. Beloborodov, I. S. Effects of fluctuations and Coulomb interaction on the transition temperature of granular superconductors. *Phys. Rev. B* **71**, 184501 (2005).
34. Xu, C. et al. Large-area high-quality 2D ultrathin Mo_2C superconducting crystals. *Nat. Mater.* **14**, 1135–1141 (2015).
35. Zhang, G. et al. Global and local superconductivity in boron-doped granular diamond. *Adv. Mater.* **26**, 2034–2040 (2014).
36. Parab, P. et al. Superconductivity in immiscible Nb–Cu nanocomposite films. *Supercond. Sci. Technol.* **30**, 055005 (2017).
37. Eley, S., Gopalakrishnan, S., Goldbart, P. M. & Mason, N. Approaching zero-temperature metallic states in mesoscopic superconductor–normal–superconductor arrays. *Nat. Phys.* **8**, 59–62 (2012).
38. Bose, S. & Ayyub, P. A review of finite size effects in quasi-zero dimensional superconductors. *Rep. Prog. Phys.* **77**, 116503 (2014).
39. Gantmakher, V. F. & Dolgopolov, V. T. Superconductor–insulator quantum phase transition. *Phys. Uspekhi* **53**, 1 (2010).

40. Altshuler, B. L. & Aronov, A. G. Electron–electron interaction in disordered conductors. in *Modern Problems in Condensed Matter Sciences* (eds. Efros, A. L. & Pollak, M.). 10 1–153 (Elsevier, 1985).

41. Finkel'Shtein, A. M. Superconductivity-transition temperature in amorphous films. *Pisma V. Zh . Eksp. Teor. Fiz.* **45**, 37–40 (1987).

42. Finkel'stein, A. M. Suppression of superconductivity in homogeneously disordered systems. *Phys. B Condens. Matter* **197**, 636–648 (1994).

Author contributions
X.Z., F.O.R., and A.S. conceived and initiated the study. A.S., P.E., and F.O.R. supervised the research. X.Z. synthesized samples. X.Z., H.L., R.S., P.O.Å.P., A.E., and P.E. performed the characterization measurements and their evaluation. X.Z. and R.S. wrote the manuscript with contributions from all the co-authors. All co-authors read, edited, and commented on successive versions of the manuscript.

Competing interests
The authors declare no competing interests.

Additional information
Supplementary information The online version contains supplementary material available at https://doi.org/10.1038/s42005-022-01059-y.

Correspondence and requests for materials should be addressed to Xiaofu Zhang, Andreas Schilling, Fabian O. von Rohr or Per Eklund.

Peer review information *Communications Physics* thanks the anonymous reviewers for their contribution to the peer review of this work. Peer reviewer reports are available.

Reprints and permission information is available at http://www.nature.com/reprints

Publisher's note Springer Nature remains neutral with regard to jurisdictional claims in published maps and institutional affiliations.